JOURNAL OF MATERIALS SCIENCE 29 (1994) 652–659

Experimental and theoretical studies on phase separations in the Fe–Al–Co ordering alloy system

T. KOZAKAI, T. MIYAZAKI‡
Centre for Cooperative Research, and ‡Department of Materials Science and Engineering, Nagoya Institute of Technology, Nagoya 466, Japan

Phase separations in iron-rich Fe–Al–Co ternary alloys were investigated by means of transmission electron microscopy, differential thermal analysis and magnetization measurement. Two kinds of phase separations have been found at 923 K; A2 + B2 and B2 + B2*. The former occurs in a tongue-shaped composition region ranging from Fe–12 at % Al–15 at % Co to Fe–35 at % Al–45 at % Co and the latter appears in the small region bordering on the Fe–Al binary side of the A2 + B2 field. These two-phase fields have theoretically been evaluated on the basis of the so-called Bragg–Williams–Gorsky model taking account of not only chemical but also magnetic interactions. The magnetic ordering accounts for the expansion of the A2 + B2 coexistent region. In the measurement of magnetic properties, large increases in coercive force, H_c, and residual magnetic flux density, B_r, were observed in the two-phase microstructures.

1. Introduction

A phase separation in an ordered solid solution is one of the important subjects in the field of material science. It has been believed that, because an ordering system has a negative interaction energy between the nearest neighbour atoms and hence has a strong tendency to form unlike atom pairs, the phase separation arising from the formation of like pairs does not occur in the ordering alloy system. Recently, however, the phase separations in ordered phases have experimentally been found for several alloys such as Fe–Si [1–3], Fe–Al [4–6], Fe–Ge [7], Fe–Ga [8], Cu–Mn–Al [9] and so on. A theoretical evaluation of the free energy for such binary systems, where the interaction energies up to higher order neighbours are taken into account, has been investigated [10], and thereby the understanding of phase separation in ordered binary alloys has rapidly been promoted. In ternary alloy systems, however, phase separations have only been investigated in a few alloy systems such as Fe–Si–Al [11], Fe–Si–V [12] and Fe–Si–Co [12] as far as we know. In a practical aspect, several iron-based ordering alloys have been reported to have good magnetic properties [13, 14]. For example, FeGaSi and FeAlGe alloys prepared by sputtering show excellent soft magnetism [13]. In this practical research, however, no microstructural investigation was performed. Most of the material properties are sensitive to the microstructure of the materials and the microstructures are mainly dominated by the phase diagram. Consequently, the phase diagram is the useful guide to develop new materials.

In recent years we have experimentally investigated the phase separations of the ternary ordering iron-based alloys and proposed the ternary phase diagrams [12]. Furthermore, we have thermodynamically calculated the phase diagrams on the basis of the Bragg–Williams–Gorsky (BWG) approximation [15, 16].

The phase separations of Fe–Al–Co ternary alloy system have previously been studied by a few workers [17, 18]. Inden [18] and co-workers have reported the phase separation of A2 into A2 and B2, while our group [17] have found the B2 + B2* phase separation in addition to the A2 + B2 separation. Thus, the phase diagram of this system is still indistinct.

In the present paper, we report experimental results on the phase separation in iron-based Fe–Al–Co alloys and propose the phase diagrams. The calculated phase diagrams on the basis of the so-called BWG approximation are shown and the effect of ferro-magnetic ordering on the phase separation is discussed thermodynamically. Finally, the magnetic properties experimentally obtained for several Fe–Al–Co alloys are discussed on the basis of relevance with the phase diagram.

2. Experimental procedure

A large number of Fe–Al–Co alloys prepared with a vacuum induction furnace were remelted in a quartz tube, 7 mm diameter, and then quenched directly on to a steel roll rotating at a high speed. The ribbon specimen obtained was about 1 mm wide and 20–30 μm thick. The ribbons were isothermally annealed at 923 K for various times up to about 26 days, and their microstructures were observed by transmission electron microscopy (TEM).

Thin foils for TEM were prepared by electropolishing in a solution of $HClO_4$ (11% by volume) and

0022–2461

CH_3COOH (89%). In the TEM observation, the incident electron beam was directed parallel to the [0 1 1] direction of the thin foil. Differential thermal analysis (DTA) was performed to obtain an outline of the two-phase boundary in the phase diagram. Energy dispersion spectroscopic (EDS) and magnetic analyses were carried out to determine the direction of the tie-line in the two-phase field. In the EDS analysis, local compositions of the microstructures were measured *in situ* with TEM, using an electron probe hole about 5 nm in size. In the thermomagnetic analysis, the specimens were heated from room temperature to 1273 K at a rate of about 1.67 $K\,s^{-1}$.

Coercive force, H_c, and residual magnetic flux density, B_r, were measured at room temperature using the vibrational sample magnetometer (VSM) at the maximum applied field of 1.19 $MA\,m^{-1}$ (15 kOe). The specimen used for measurement of magnetic properties was cylindrical shaped, 6 mm diameter and 5 mm high, and the magnetic field was applied parallel to the direction axis of the cylindrical sample.

3. Results

3.1. Electron microscopic observations

TEM microstructures were observed for several alloys annealed at 923 K, mainly for more than 20 days. In this section four typical microstructures are shown.

Fig. 1 shows the electron micrograph of Fe–15 at % Al–14 at % Co alloy (alloy T) annealed at 923 K for 1.99×10^6 s (23 days). In a bright-field image (a), many cuboid precipitates are observed, while in a dark-field image (b), taken from the 1 0 0 ordered spot, these precipitates are brightly illuminated. The alloy thus shows a microstructure where ordered B2 cubes disperse in a disordered A2 matrix phase. Micrographs of Fe–24 at % Al–19 at % Co alloy (W) annealed at 923 K for 2005×10^3 s (24 days) are shown in Fig. 2. Because cuboid particles are brightly illuminated in the dark matrix (b), the A2 + B2 phase separation also occurs in this alloy.

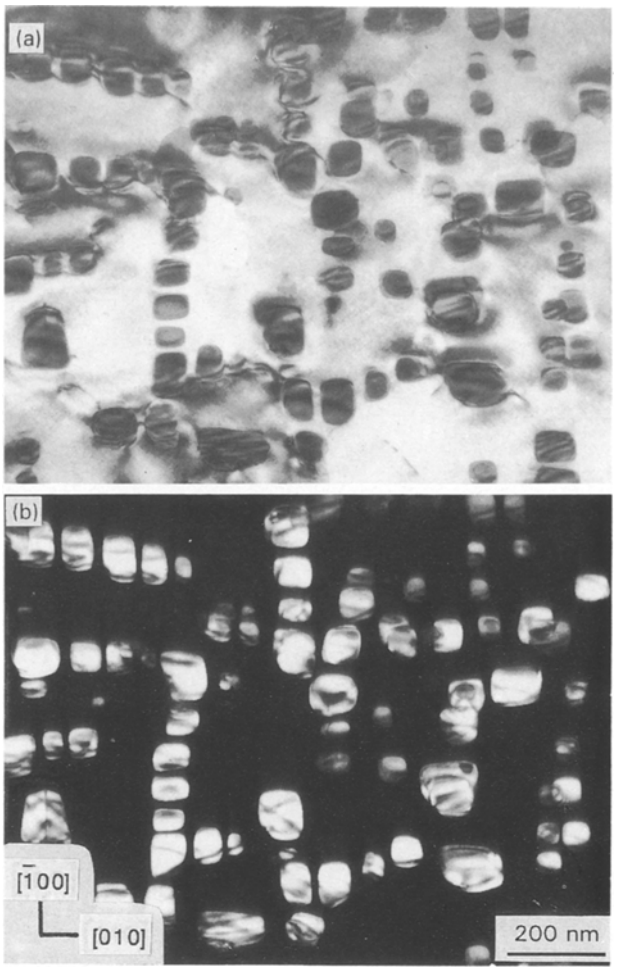

Figure 1 Transmission electron micrographs of Fe–15 at % Al–14 at % Co alloy (T) annealed at 923 K for 1.99×10^6 s (23 days). (a) Bright-field and (b) dark-field images from a 1 0 0 ordered spot.

Fig. 3 shows a 1 0 0 dark-field image of Fe–21 at % Al–11 at % Co alloy (I) annealed at 923 K for 1886×10^3 s (21 days). It is well known that there are two kinds of ordered phases having different brightness. One is cuboid precipitate and the other is

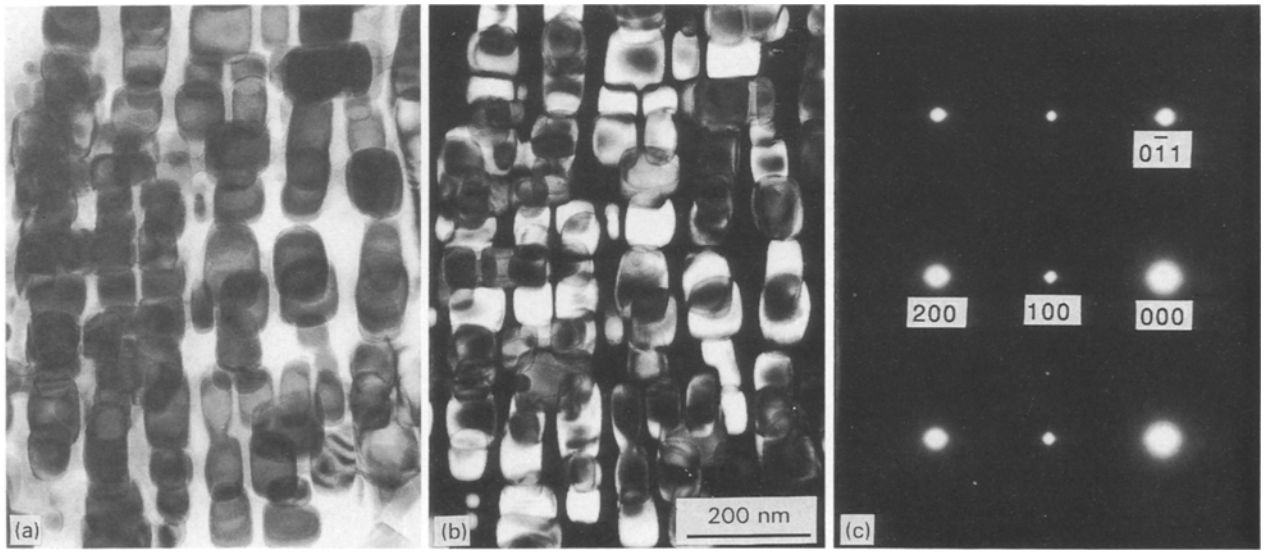

Figure 2 Transmission electron micrographs of Fe–24 at % Al–19 at % Co alloy (W) annealed at 923 K for 2005×10^3 s (24 days). (a) Bright-field, (b) dark-field images from a 1 0 0 ordered spot and (c) (0 1 1) diffraction pattern.

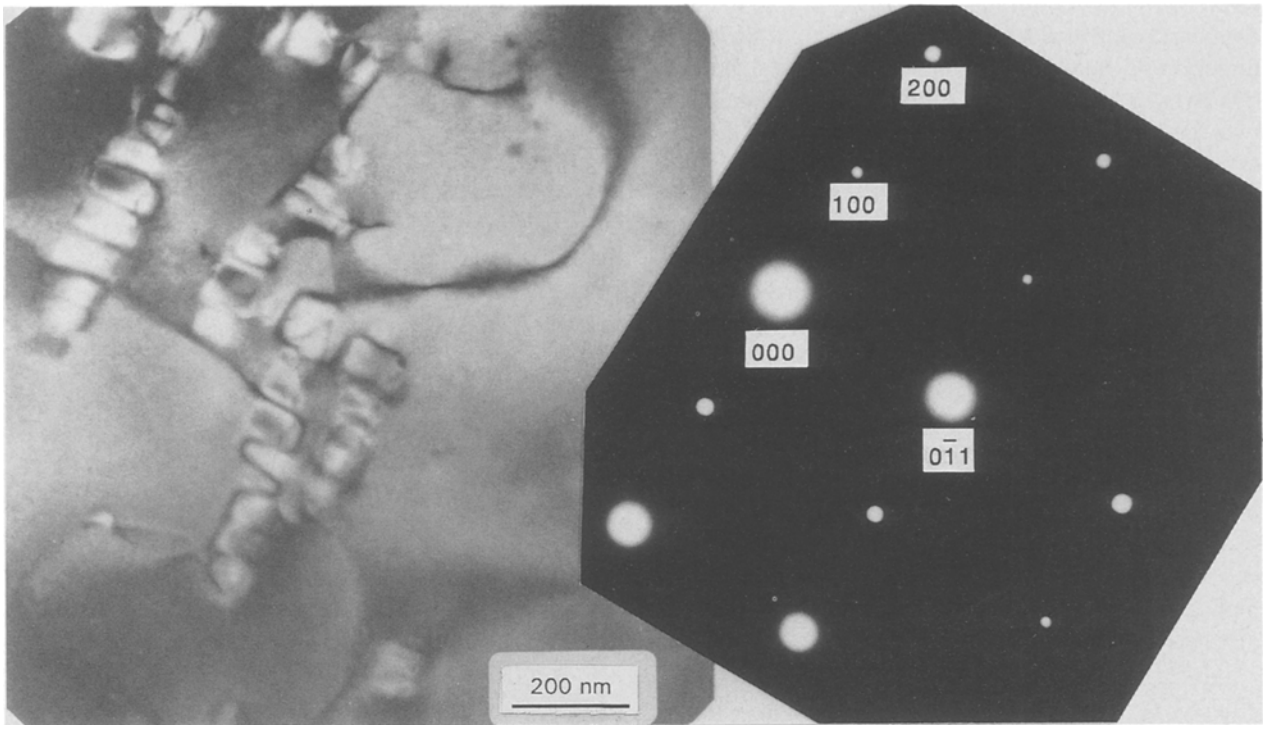

Figure 3 (a) Dark-field image from a 1 0 0 ordered spot and (b) (0 1 1) electron diffraction pattern of Fe–21 at % Al–11 at % Co alloy (I) annealed at 923 K for 1886×10^3 s (21 days), showing two kinds of ordered phases.

the matrix with anti-phase boundary (APB). In the electron diffraction pattern, only one kind of ordered spot, 1 0 0 spot, is observed and no other type of ordered spot, such as DO_3 type 1/2, 1/2, 1/2 superlattice spot, is ever recognized. Therefore, the microstructure results in B2 + B2* phase separation.

When an Fe–35 at % Al–35 at % Co alloy (Q) is annealed at 923 K for 2246×10^3 s (26 days), the microstructure shown in Fig. 4 is obtained. Rod-shaped precipitates are observed as dark parts in the dark-field image (b). This indicates that disordered A2 phases precipitate in B2 ordered matrix.

3.2. Phase diagrams

On the basis of many observations of microstructures, an isothermal equilibrium phase diagram at 923 K was determined as shown in Fig. 5. A2 + B2 two-phase field expands from A2/B2 transition line of the iron-rich corner to the central part of the Gibbs triangle like a tongue, and the B2 + B2* field exists adjacent to the aluminium-rich side of the A2 + B2 region.

In order to determine the change of the coexistent field with temperature, we undertook a DTA analysis. Fig. 6 shows the DTA curve of Fe–22 at % Al–13 at % Co alloy (Y), where an endothermic peak is recognized at 983 K. This indicates that precipitation of B2 phase from A2 begins to occur at T_1 and dissolution of B2 starts roughly at 983 K. Thus, the boundary temperature of the single/two-phase is estimated to be 983 K for this alloy. Fig. 7 represents the boundary temperatures experimentally obtained from the endothermic peaks. With decrease of temperature, the two-phase coexistent field expands, particularly to

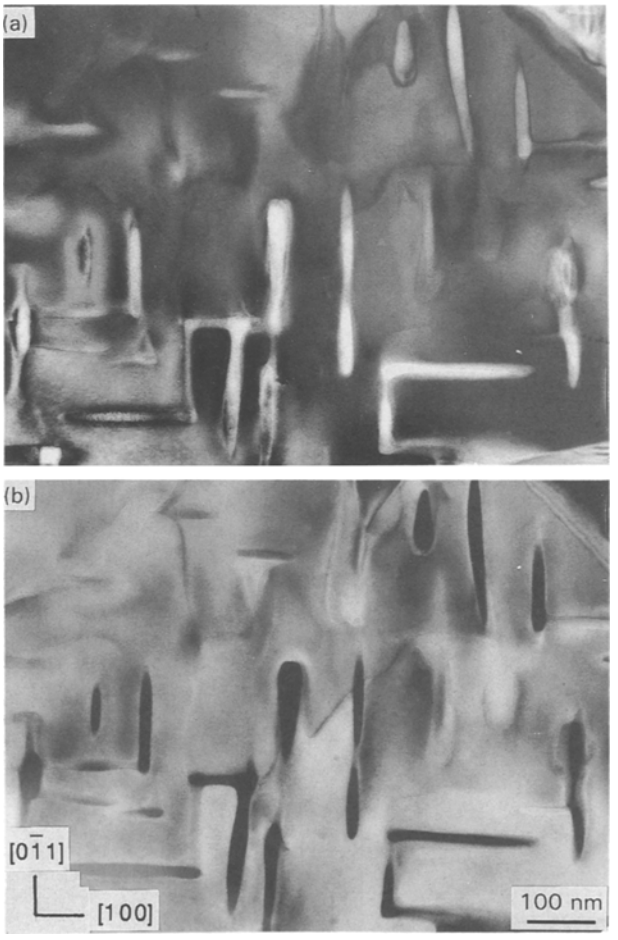

Figure 4 (a) Bright-field and (b) 1 0 0 dark-field images of Fe–35 at % Al–35 at % Co alloy (Q) annealed at 923 K for 2246×10^3 s (26 days). Rod-shaped disordered A2 phases precipitate in the matrix B2 ordered phase.

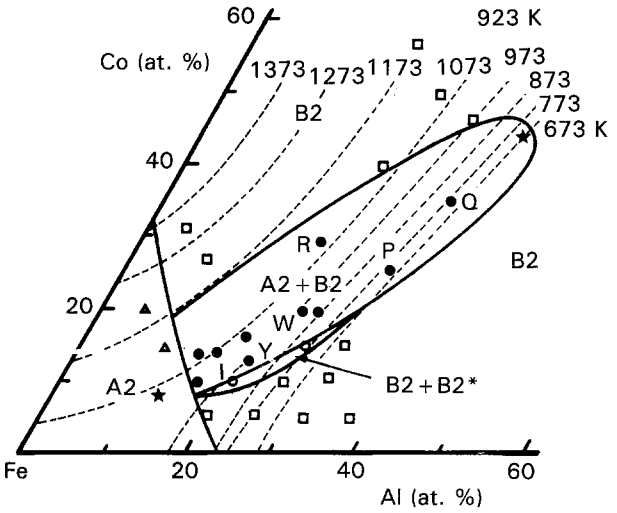

Figure 5 An isothermal section of the experimental phase diagram of the iron-rich corner of the Fe–Al–Co ternary system at 923 K. (△) A2, (□) B2, (●) A2 + B2, (○) B2 + B2*. Asterisks indicate the chemical compositions of B2 and A2 phases calculated from the EDS spectrum of Fig. 8.

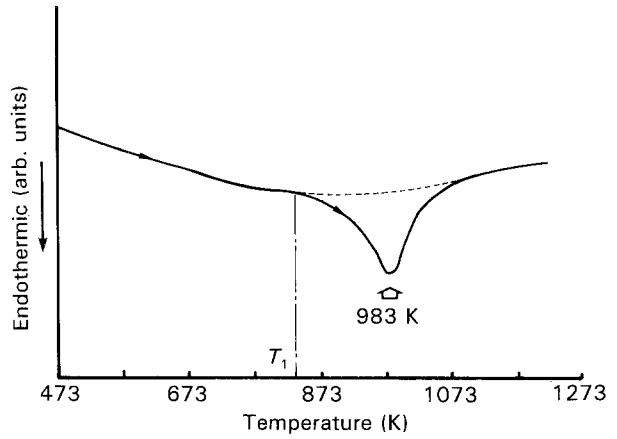

Figure 6 DTA curve during heating of Fe–22 at % Al–13 at % Co alloy (Y), showing an endothermic peak at about 983 K. Heating rate 0.25 K s^{-1}.

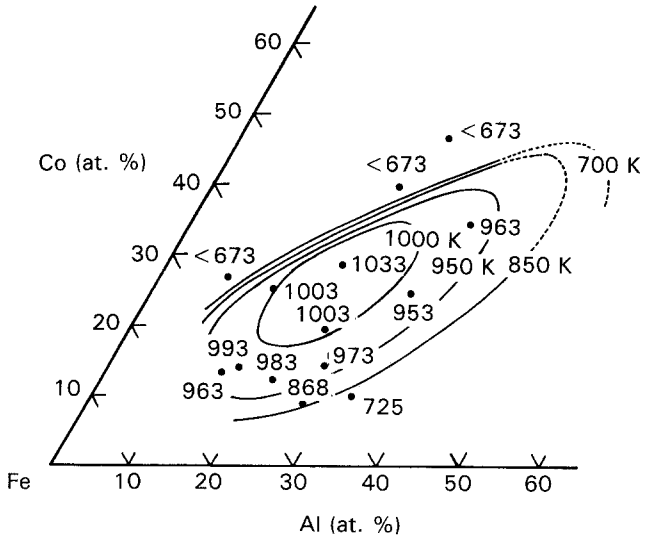

Figure 7 Single/two-phase boundary temperatures from DTA peaks and two-phase region at various temperatures.

the Fe–Al binary side, while the phase boundary shows little shift in the Fe–Co binary side.

3.3. Tie-line and decomposition path of A2 + B2 phase separation

According to the phase diagram shown in Fig. 5, the direction of the tie-line of A2 + B2 phase separation is thought to be roughly parallel to the line connecting pure iron with the central part of the ternary phase diagram. This was, in fact, experimentally confirmed by *in situ* energy dispersion spectroscopic (EDS) chemical analyses for A2 and B2 phases. Fig. 8 shows the EDS X-ray spectrum taken from the microstructure of the alloy W (see Fig. 2). Cobalt and aluminium atoms are concentrated into the B2 ordered precipitate, while iron atoms are enriched into A2. Copper peaks are due to the grid supporting the thin foil. According to the thin-film approximation proposed by Zaluzec [19], the average chemical compositions of A2 matrix and B2 precipitate are estimated to be Fe–12.1 at % Al–9.4 at % Co and Fe–37.4 at % Al–43.9 at % Co, respectively, marked with asterisks in Fig. 5.

Although the tie-line was determined from the EDS analysis, as mentioned above, the path of phase decomposition is still unknown. For the estimation of the decomposition path, the change in Curie temperatures with progress of phase decomposition was measured for the alloys R and W, as shown in Fig. 9. Equi-Curie temperature lines, shown as broken curves in Fig. 5 [17], are nearly parallel to the tie-line. If the alloy begins to decompose initially along the direction normal to the tie-line, that is normal to the equi-Curie temperature line, the Curie temperature of the alloy

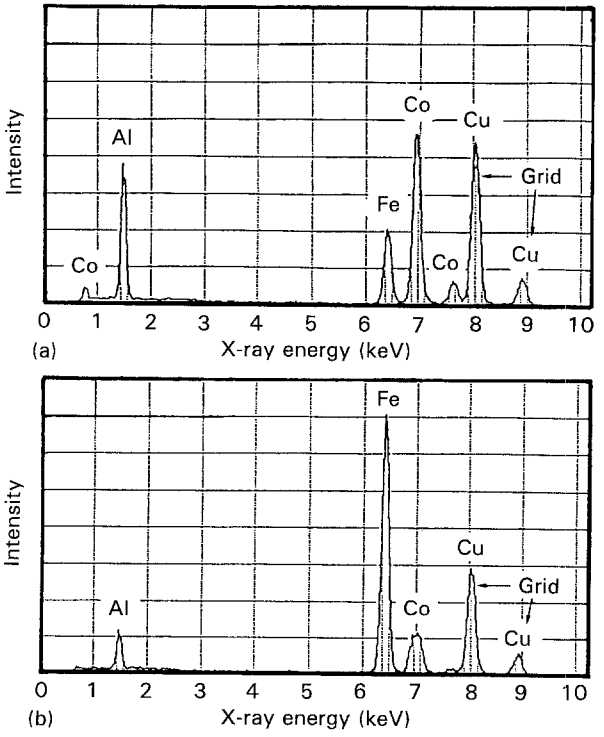

Figure 8 EDS X-ray spectrum from (a) B2 and (b) A2 phases of Fe–24 at % Al–19 at % Co alloy (W) annealed at 923 K for 2×10^6 s.

must rapidly rise in the early stage of the phase decomposition. However, the Curie temperatures in alloys W and R rise gradually with annealing. Therefore, it is concluded that the phase decomposition progresses nearly along the tie-line throughout the phase decomposition.

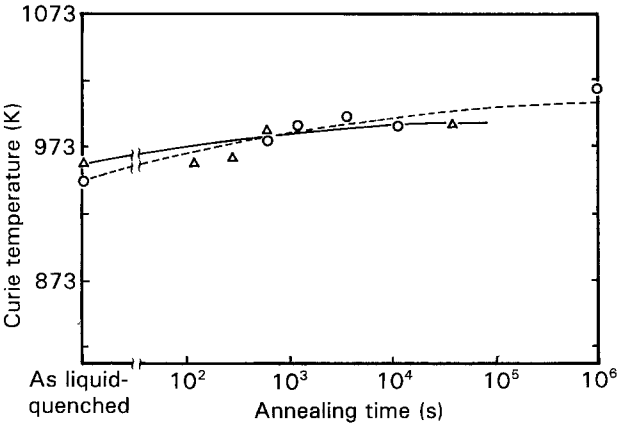

Figure 9 Changes in Curie temperatures with annealing at 923 K of (○) Fe–22 at % Al–29 at % Co (R) and (△) Fe–24 at % Al–19 at % Co (W) alloys, which are initially as-liquid quenched.

4. Calculations of ternary phase diagrams based on the Bragg–Williams–Gorsky model

4.1. Theoretical background

The calculation model is only briefly mentioned here because it has already been shown in detail in our previous papers [15, 16].

In order to describe the atomic configurations of B2 and DO_3 ordered structures in bcc ternary alloy, we divided the unit cell of DO_3 superlattice into four fcc sublattices I, II, III and IV, and defined six independent order parameters given by the following equations

$$\begin{aligned} X_A &= (P_A^I + P_A^{II} - P_A^{III} - P_A^{IV})/(P_A^I + P_A^{II} + P_A^{III} + P_A^{IV}) \\ Y_A &= (P_A^{III} - P_A^{IV})/(P_A^{III} + P_A^{IV}), \\ Z_A &= (P_A^I - P_A^{II})/(P_A^I + P_A^{II}) \\ X_B &= (P_B^I + P_B^{II} - P_B^{III} - P_B^{IV})/(P_B^I + P_B^{II} + P_B^{III} + P_B^{IV}) \\ Y_B &= (P_B^{III} - P_B^{IV})/(P_B^{III} + P_B^{IV}), \\ Z_B &= (P_B^I - P_B^{II})/(P_B^I + P_B^{II}) \end{aligned} \quad (1)$$

where P_i^L is the occupation probability of atom i on the sublattice L. In addition to these atomic order parameters, a parameter q_i is introduced to express the magnetic ordering between spins. The occupation probability of atom i having up or down spin on the sublattice L is given by

$$P_{i\uparrow}^L = P_i^L(1 + q_i)/2,\ P_{i\downarrow}^L = P_i^L(1 - q_i)/2,\ P_i^L = P_{i\uparrow}^L + P_{i\downarrow}^L \quad (2)$$

Here, the ferromagnetic and paramagnetic states are represented by $q_i = \pm 1$ and $q_i = 0$, respectively.

The phase stability of an alloy is generally affected by not only atomic ordering but also magnetic ordering [20]. Therefore, when the alloy contains a ferromagnetic element, the magnetic interchange energy, J_{ij}, between the magnetic moments should be introduced in addition to the atomic interchange energy, W_{ij}. The kth nearest neighbour magnetic interchange energy, J_{ij}^k, is defined by

$$J_{ij}^k = (V_{i\uparrow j\uparrow} - V_{i\uparrow j\downarrow})/2 \qquad (k = 1, 2) \quad (3)$$

where $V_{i\uparrow j\uparrow}$ and $V_{i\uparrow j\downarrow}$ are the bonding energies of i–j atom pairs with parallel and antiparallel spins, respectively. When $J_{ij}^k < 0$, the alloy is in a ferromagnetic state.

The configurational free energy, F_k, of the A–B–C ternary solid solution, taking into account a pairwise interaction approximation up to the second nearest neighbour, is given by the following equation

$$\begin{aligned} F_k = {} & U^0 - N\sum C_iC_j[4(W_{ij}^{(1)} + M_{ij}^{(1)}) + 3(W_{ij}^{(2)} + M_{ij}^{(2)})] \\ & + N\sum C_i(4J_{ii}^{(1)} + 3J_{ii}^{(2)})q_i^2 + N\sum C_iC_jX_iX_j[4(W_{ij}^{(1)} + M_{ij}^{(1)}) - 3(W_{ij}^{(2)} + M_{ij}^{(2)})] \\ & + (3N/2)\sum C_iC_j[(1 - X_i)(1 - X_j)Y_iY_j + (1 + X_i)(1 + X_j)Z_iZ_j](W_{ij}^{(2)} + M_{ij}^{(2)}) \\ & + kNT\sum C_i\ln C_i + (kNT/2)\sum C_i[(1 - X_i)\ln(1 - X_i) + (1 + X_i)\ln(1 + X_i)] \\ & + (kNT/4)\sum\{C_i(1 - X_i)[(1 + Y_i)\ln(1 + Y_i) + (1 - Y_i)\ln(1 - Y_i)] \\ & + C_i(1 + X_i)[(1 + Z_i)\ln(1 + Z_i) + (1 - Z_i)\ln(1 - Z_i)]\} \\ & + kNT\sum m_iC_i\{[(1 + q_i)/2]\ln[(1 + q_i)/2] + [(1 - q_i)/2]\ln[(1 - q_i)/2]\} \end{aligned} \quad (4)$$

$$M_{ij}^{(1)} = -2J_{ii}^{(1)}q_iq_j + J_{ii}^{(1)}q_i^2 + J_{jj}^{(1)}q_j^2$$

$$M_{ij}^{(2)} = -2J_{ij}^{(2)}q_iq_j + J_{ii}^{(2)}q_i^2 + J_{jj}^{(2)}q_j^2 \qquad i, j = \text{A, B, C.}$$

4.2. Calculation of Fe–Al–Co ternary phase diagrams

4.2.1. Assessment of atomic and magnetic interchange energies

Calculation of the Fe–Al–Co ternary phase diagram requires numerical values of atomic and magnetic interchange energies for three binary subsystems Fe–Al, Fe–Co and Al–Co. The numerical values of interchange energies used in the calculation are summarized in Table I. (According to Inden [10], numerical values of interchange energies are dependent on a statistical model. The values in Table I are corrected by using the method proposed by Inden.)

The iron-rich part of the Fe–Al binary phase diagram has been analysed by Oki *et al.* [6]. They examined the phase diagram on the basis of the BWG

TABLE I Numerical values of interchange energies used in the calculation of phase diagrams in Fig. 10.

	$W^{(1)}$	$W^{(2)}$	$J^{(1)}$	$J^{(2)}$	Ref.
Fe–Al	1100 k	550 k	–	–	[6]
Fe–Co	410 k	0 k	–	–	[21]
Al–Co	2660 k	1110 k	–	–	[25]
Fe–Fe	–	–	− 197 k	67 k	[6]
Co–Co	–	–	− 125 k	− 67 k	
Fe–Co	–	–	− 200 k	0 k	

$k = 1.38 \times 10^{-23}$ J

approximation containing the magnetic interactions up to the second nearest neighbours and estimated the atomic interchange energies $W^{(1)}_{FeAl}$, $W^{(2)}_{FeAl}$ and the magnetic interchange energies $J^{(1)}_{FeFe}$, $J^{(2)}_{FeFe}$ as shown in Table I.

For the Al–Co system, Ackermann [25] has recently evaluated atomic interchange energies $W^{(1)}_{AlCo}$, $W^{(2)}_{AlCo}$ from the experimental values of A2/B2 critical temperatures in several Fe–Al–Co alloys.

Inden [21] and Inden and Meyer [22] have performed the analysis for the Fe–Co binary system by considering the magnetism, and estimated two atomic interchange energies, $W^{(1)}_{FeCo}$, $W^{(2)}_{FeCo}$, and three magnetic interchange energies, $J^{(1)}_{FeFe}$, $J^{(1)}_{FeCo}$, $J^{(1)}_{CoCo}$. In their calculations, the magnetic interchange energy was considered only for the first nearest neighbour spins, as described above. In the present study, however, because the magnetic interaction is taken into account up to the second nearest neighbour distance, new magnetic interchange energies need to be evaluated. Adopting the atomic interchange energies $W^{(k)}_{FeCo}$ ($k = 1, 2$) determined by Inden [21], and the magnetic interchange energies $J^{(k)}_{FeFe}$ ($k = 1, 2$) derived by Oki *et al.* [6], we re-estimated the other magnetic interchange energies $J^{(1)}_{FeCo}$, $J^{(2)}_{FeCo}$, $J^{(1)}_{CoCo}$ and $J^{(2)}_{CoCo}$ based on the critical temperature of A2/B2 transition [23] and the Curie temperature [22] experimentally obtained for the Fe–Co binary system.

4.2.2. Isothermal ternary phase diagrams

The iron-rich part of the ternary equilibrium phase diagrams calculated at 923, 873 and 800 K, are shown in Fig. 10. The A2 + B2 coexistent fields appear at 923 K in two regions: one spreads from the iron-rich region towards the CoAl intermetallic compound (hereafter this field is called A2 + B2 (I)), and the other exists as a small region near the Fe–Al binary system (A2 + B2 (II)). A coexistent field B2 + B2* lies adjacent to the A2 + B2 (I). The A2 + B2 (I) and B2 + B2* fields agree with the experimental result (see Fig. 5), although the A2 + B2 (I) field is smaller than the experimental one. In the phase diagrams at lower temperatures (Fig. 10b, c), not only the two-phase regions such as A2 + DO_3 and DO_3 + DO_3^*, but also a three-phase coexistent field appears.

The magnetic transformation line at 923 K lies nearly on the boundary between A2 + B2 (I) two-phase and B2 single fields, as shown in Fig. 10a. This implies that the magnetic ordering has a great influence on the phase separation, particularly on the A2 + B2 (I) phase separation. In fact, when the magnetic interaction is not taken into account in the calculation of the phase diagram, the A2 + B2 (I) region shrinks and shifts to the Fe–Co binary side and the other coexistent regions disappear, as is recognized by comparing the solid line and the dotted line in Fig. 10a. It is, therefore, concluded that the magnetic ordering causes the expansion of the A2 + B2 (I) two-phase region.

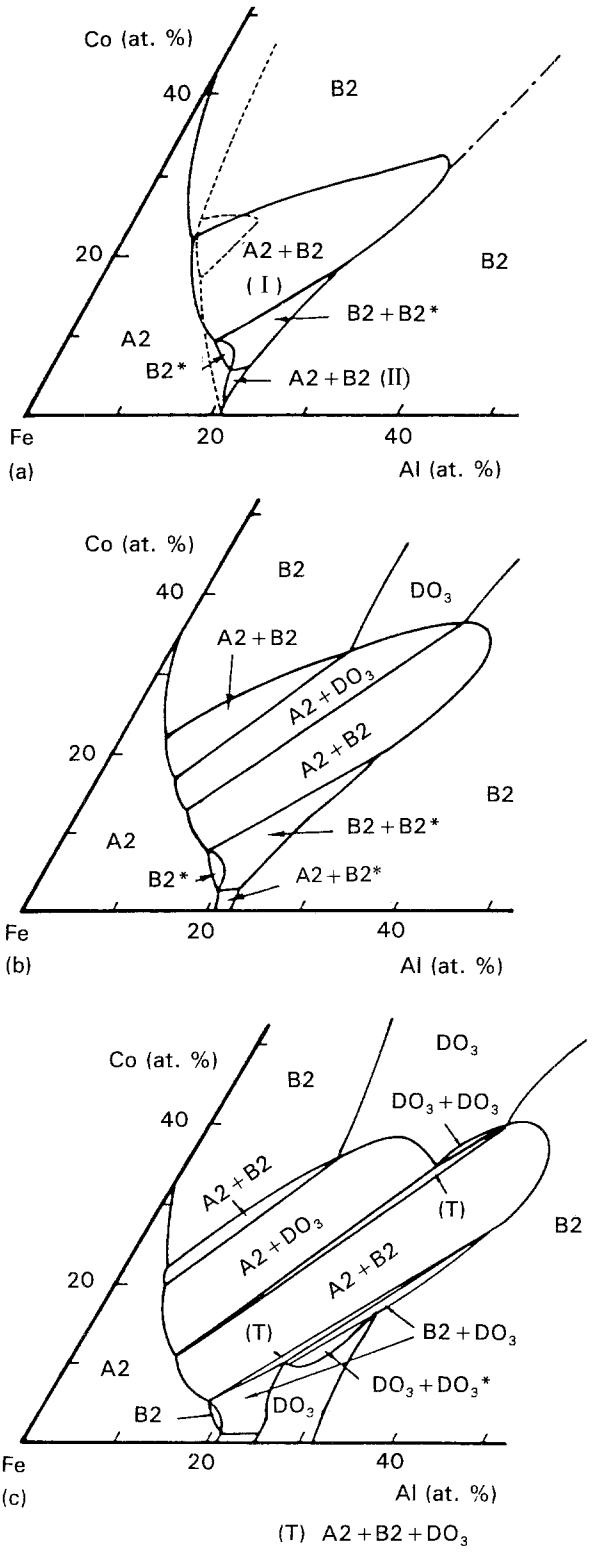

Figure 10 The iron-rich part of the calculated phase diagrams for the ternary Fe–Al–Co system. (a) 923 K, (b) 873 K and (c) 800 K. (· · ·) Phase boundary in a paramagnetic state, (— · —) magnetic transformation line.

Colinet *et al.* [24] recently calculated the Fe–Al–Co ternary phase diagrams using the cluster variation method (CVM). Because their calculations are based on the tetrahedron approximation containing the multiple correlations, the results might be more precise than our calculations with the BWG point approximation. As mentioned above, however, our results are approximately coincident with the phase diagram obtained experimentally.

5. Magnetic properties

The properties of materials are generally affected by the phase separation. In this section the magnetic properties such as the coercive force, H_c, and the residual magnetic flux density, B_r, are shown as functions of alloy composition and annealing time.

The alloys were solution-treated at 1073 K for 1.44×10^3 s (4 h) and then annealed at 923 K for 21.6×10^3 s (60 h). The increments of H_c with annealing, $\Delta H_c (= H_{c923K} - H_{c1073K})$, are described in the phase diagram (see Fig. 11). The alloys without phase separation hardly change in H_c, while the alloys with phase separation such as P, W, and Q, show a fairly large increase in H_c. In particular, the Fe–35 at % Al–35 at % Co alloy (Q), shows the largest increase of 35.6 kA m^{-1}. Such a composition dependence was also recognized in the changes in B_r for the same three alloys. These experimental results clearly show that the phase separation, and hence the morphology of microstructure, greatly affect the magnetic properties of the alloy.

Changes in H_c and B_r of the alloy Q with annealing time are shown in Fig. 12. H_c and B_r begin to increase at about 20×10^3 s annealing time and reach maxima at about 600×10^3 s. Fig. 13a–c are TEM 1 0 0 dark-field images of the alloy Q annealed at 923 K for 86.4×10^3 s, 586.8×10^3 s and 1209.6×10^3 s, respectively. Disordered A2 phases precipitate in the ordered B2 matrix. The A2 precipitates grow in size with annealing and their shape changes from round cuboid to plate or rod-shaped.

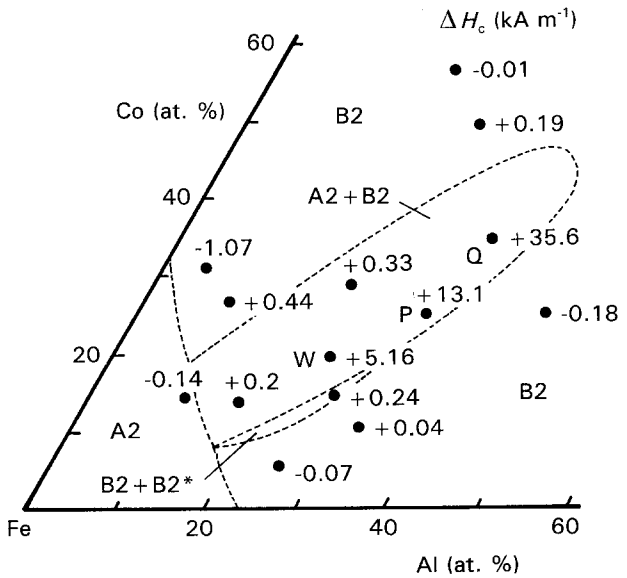

Figure 11 Increases, $\Delta H_c (= H_{c923K} - H_{c1073K})$, in coercive force H_c on annealing at 923 K.

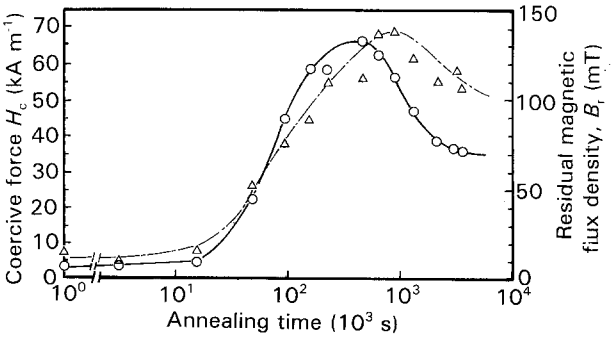

Figure 12 Changes in (○) H_c and (△) B_r of Fe–35 at % Al–35 at % Co alloy (Q) during annealing at 923 K.

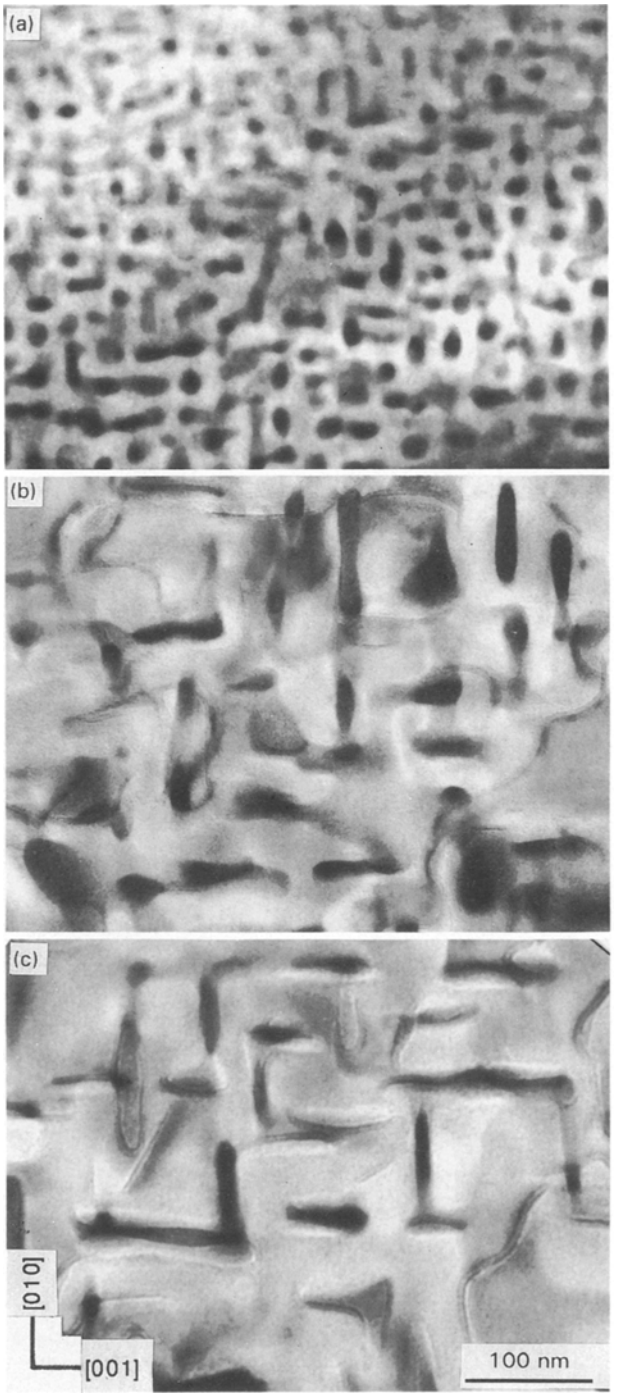

Figure 13 1 0 0 dark-field images of Fe–35 at % Al–35 at % Co alloy (Q) annealed at 923 K for (a) 86.4×10^3 s (24 h), (b) 586.8×10^3 s (163 h) and (c) 1209.6×10^3 s (14 days).

On the basis of the phase diagram shown in Fig. 5, the experimental results above described are explained as follows: because the phase separation proceeds along the tie-line, the two coexistent phases should be A2 phase with high Curie temperature, T_c, and B2 with low T_c. The A2 phase is ferromagnetic while the B2 phase is almost paramagnetic because of a small saturation magnetization. According to the theory of magnetism, the microstructure where ferromagnetic particles are embedded in a paramagnetic matrix gives good hard magnetic properties and, in fact, such a microstructure has been observed in the permanent magnets such as Alnico and Fe–Cr–Co alloys. Therefore, the precipitation of A2 from the B2 matrix must cause the improvement in H_c and B_r in alloy Q. The phase diagram indicates that the volume fraction of B2 phase of alloy P or W is smaller than that for alloy Q, and in alloy W the paramagnetic B2 particles are embedded in a ferromagnetic A2 matrix (see Fig. 2). This is the reason why ΔH_c of alloy P or W is smaller than that of alloy Q.

6. Conclusions

The phase separation and phase diagram were experimentally investigated for Fe–Al–Co ternary alloys using TEM, DTA, EDS and magnetic analysis. The results obtained have been thermodynamically discussed on the basis of the BWG approximation. Magnetic properties of the phase-separated alloys were also measured. The following results were obtained.

1. Two kinds of phase separations occur at 923 K, A2 + B2 and B2 + B2*; the former occurs in a large composition region from Fe–12 at % Al–15 at % Co to the central part of the Gibbs triangle and the latter appears on the Fe–Al binary side.
2. The A2 + B2 and B2 + B2* two-phase fields calculated based on the BWG model are approximately coincident with the regions determined experimentally.
3. The A2 + B2 field is enlarged by magnetic ordering.
4. Increases of coercive force and residual magnetic flux density with annealing are observed in the alloys whose compositions are located in the high solute content area of the A2 + B2 field.

Acknowledgements

The authors thank Dr M. Doi and Mr Y. Koyama, Nagoya Institute of Technology, for discussions and Mr T. Katoh for experimental and calculational assistance. This work was financially supported in part by a Grant-in-Aid for Scientifc Research (C) from the Ministry of Education, Japan.

References

1. G. INDEN and W. PITSH, *Z. Metallkde* **63** (1972) 253.
2. G. SCHLATTE and W. PITSH, *ibid.* **66** (1975) 660.
3. P. R. SWANN, L. GRANAS and B. LEHTINEN, *Metal Sci.* **9** (1975) 90.
4. S. M. ALLEN and J. W. CAHN, *Acta Metall.* **23** (1975) 1017.
5. P. R. SWANN, W. R. DUFF and R. M. FISHER, *Metall. Trans.* **3** (1972) 409.
6. K. OKI, H. SAGANE and T. EGUCHI, *Jpn J. Appl. Phys.* **13** (1974) 753.
7. H. ENOKI, K. ISHIDA and T. NISHIZAWA, *Metall. Trans.* **18A** (1987) 949.
8. K. UDO, K. OKI and T. EGUCHI, *J. Jpn Inst. Metals* **49** (1985) 337.
9. M. BOUCHARD and G. THOMAS, *Acta Metall.* **23** (1975) 1485.
10. G. INDEN, *Z. Metallkde* **66** (1975) 577; 648.
11. T. MIYAZAKI, T. TSUZUKI and T. KOZAKAI, *J. Mater. Sci.* **21** (1986) 2557.
12. T. KOZAKAI, P. Z. ZHAO and T. MIYAZAKI, in "Proceedings of the 1st Japan International SAMPE Symposium" 28 November–1 December 1989, Chiba, p. 139.
13. K. HAYASHI, M. HAYAKAWA, W. ISHIKAWA, Y. OCHIAI, Y. IWASAKI and K. ASO, *J. Appl. Phys.* **64** (1988) 772.
14. K. HAYASHI, M. HAYAKAWA, W. ISHIKAWA, Y. OCHIAI, H. MASTUDA, Y. IWASAKI and K. ASO, *ibid.* **61** (1987) 3514.
15. M. FUKAYA, P. Z. ZHAO, T. KOZAKAI and T. MIYAZAKI, *J. Mater. Sci.* **25** (1990) 522.
16. M. FUKAYA, T. KOZAKAI and T. MIYAZAKI, *ibid.* **26** (1991) 5420.
17. T. MIYAZAKI, K. ISOBE, T. KOZAKAI and M. DOI, *Acta Metall.* **35** (1987) 317.
18. G. INDEN, in "Materials Science and Technology", Vol. 5, edited by R. W. Cahn *et al.* (VCH Press, Weinheim, 1991) p. 497.
19. N. J. ZALUZEC, in "Introduction to Analytical Electron Microscopy", edited by J. J. Hren *et al.* (Plenum Press, New York, 1979) p. 121.
20. G. INDEN, *Physica* **103B** (1981) 82.
21. *Idem, Phys. Status Solidi. (a)* **56** (1979) 177.
22. G.INDEN and W. O. MEYER, *Z. Metallkde* **66** (1975) 725.
23. J. A. OYEDELE and M. F. COLLINS, *Phys. Rev. B* **16** (1977) 3208.
24. C. COLINET, G. INDEN and R. KIKUCHI, *Acta Metall.* **41** (1993) 1109.

Received 1 May 1992
and accepted 5 March 1993